中國機械工程學刊第四十一卷第五期第 551~563 頁(民國一百零九年)
Journal of the Chinese Society of Mechanical Engineers, Vol.41, No.5, pp 551~563 (2020)

Optimal Design of Investment Casting System for a Stuffing Box with Pedestal of Centrifugal Pump: Computer Simulations and Experimental Verification

Jenn-Kun Kuo*, Pei-Hsing Huang**, Yu-Ting Tsai***, Zhong Qi****and Chuen-Shii Chou*****

Keywords：investment casting, centrifugal pump, stuffing box with pedestal, retained melt modulus, Niyama criterion.

ABSTRACT

The stuffing box with pedestal (SBP) is a major component in centrifugal pumps (CPs). It is responsible for the transfer of load generated in the CP to the baseplate of the pump and finally to the ground. SBPs are usually fabricated using investment casting; however, this process is prone to residual casting defects, which can reduce mechanical strength and increase the likelihood of crack formation following long-term usage. In this study, the AnyCasting numerical simulation software package was used to optimize the investment parameters for the casting of an SBP in SUS304 alloy. Optimization efforts targeted the shrinkage cavity (based on retained melt modulus) and porosity defects (based on Niyama criterion). The results of preliminary simulations and experiments informed the establishment of five casting schemes for subsequent simulation. We used virtual thermo-dynamic sensors to determine the rate and direction of solidification in the mold cavity, and also investigated variations in the velocity of the molten metal at the inlets of the gating system as a function of time. The optimal casting parameters derived in simulations were assessed by fabricating an SBP via investment casting in a domestic foundry. Nondestructive testing based on X-ray analysis revealed none of the detrimental defects commonly associated with this type of casting.

Paper Received August, 2020. Revised September, 2020, Accepted September, 2020, Author for Correspondence: Chuen-Shii Chou.

* *Professor, Department of Greenergy, National University of Tainan, Tainan, 70005, Taiwan*
** *Professor, Department of Mechanical Engineering, National Yunlin University of Science and Technology, Yunlin 64002, Taiwan*
*** *Associate Professor, Bachelor's Program in Precision System Design, Feng Chia University, Taichung 40724, Taiwan*
**** *Gradnate Student, Department of Mechanical Engineering, National Pintung University of Science and Technology, Pingtung 91201, Taiwan*
***** *Professor, Department of Mechanical Engineering, National Pintung University of Science and Technology, Pingtung 91201, Taiwan*

INTRODUCTION

Centrifugal pumps (CPs) are used to transport a variety of fluids (e.g., freshwater, sewage, flammable liquids, acids, and caustics) in a variety of applications (e.g., fire security sprinkler systems, power generation plants, agriculture irrigation, and industry). CPs operate by converting rotational kinetic energy (from an engine or electric motor) into the hydrodynamic energy of the fluid flow (Sanders, 2015). Thus, CPs can be regarded as a dynamic machine system, in which centrifugal force is used to pump liquids from a lower to a higher level of pressure (Forsthoffer, 2011). CPs require regular maintenance due to wear associated with continuous loading.

CPs comprise two main components: an impeller (rotor) imparting centrifugal force to the fluid, and a fixed diffuser (stator) guiding the flow to the discharge. The most important element in the design and performance of a pump is the geometry of the impeller (Matlakala et al., 2019). A certain amount of vibration and noise is inevitable in any CP, due to mechanical causes (e.g., unbalanced rotating components), hydraulic causes (e.g., turbulence in the system), and peripheral causes (e.g., harmonic vibration from nearby equipment or drivers) (Birajdar et al., 2009). Through the stuffing box and attached pedestal, the load is transferred to the baseplate of the pump and finally into ground (Moroe and Palmer, 2002; Rushabh et al., 2017). The stuffing box with pedestal (SBP) is usually fabricated using investment casting; however, this process is prone to residual casting defects, which can reduce mechanical strength and increase the likelihood of crack formation following long-term usage. Sudden SBP breakage also poses a serious safety hazard. Figures 1(a)-(d) illustrate some of the defects typically observed in

SBPs fabricated using investment casting, including cavitation at the surface of the SBP and surface shrinkage porosity at the joint between the cylindrical stuffing box and supporting pedestal. Eliminating these types of defects requires accurate predictions related to shrinkage during solidification (Kuo et al., 2017; Zhang and Chen, 2005; Zhou et al., 2004; Huang and Guo, 2015); unfortunately, literature pertaining to the optimal design of investment casting systems for SBPs is limited.

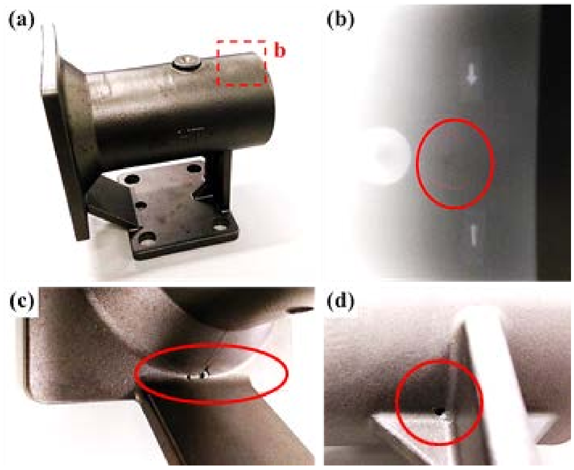

Fig. 1. Cavitation observed at the surface of SBP: (a) finished product of casting, (b) enlarged image showing cavitation defect, (c)-(d) surface shrinkage porosity at the joint between the cylindrical stuffing box and the supporting pedestal.

In the past, research on casting parameters was based on trial-and-error, which tends to be imprecise, time-consuming, and expensive. It is difficult to formulate reasonable predictions pertaining to the formation of the casting defects, due to the fact that the flow of molten metal through the cavity and the direction of solidification cannot be observed. Computer-aided engineering (CAE) software has been developed to enable predictions of where and how defects are likely to form as well as the direction of solidification (Kalpakjian and Schmid, 2003; Groover, 2007). These simulation systems have largely eliminated the costs and imprecision associated with conventional trial-and-error methods.

Beckermann and Carlson (2008) used the Niyama porosity criterion to predict shrinkage-related leaks in nickel-based and high-nickel steel alloy castings. The Niyama porosity criterion describes the pressure drop in the mushy region as an inverse function of $G/R^{1/2}$, where symbols G and R respectively refer to the thermal gradient and solidification rate at the end of the solidification process (Niyama et al., 1982). Guo et al. (2015) formulated predictions related to micro-pore formation in Ni-based super alloy castings. Liao et al. (2011) performed numerical simulation on the thermal stress fields involved in casting steel. Budavari and Molnar (2014) reported on control volume simulations to make predictions pertaining to directional solidification in a large-scale steel casting. With a focus on the retained melt modulus (RMM), Huang et al. (2014) and Kuo et al. (2019) used AnyCasting software to analyze the formation of investment casting defects in steam generator supports, cladding thin-plate heaters, and stainless steel exhaust manifolds.

Note that no previous studies have focused on optimizing the investment casting of SBPs for CPs. In this study, we used numerical simulations based on RMM and the Niyama criterion to analyze defect patterns associated with the casting of SBP in SUS304. The optimal casting parameters derived in simulations were assessed by fabricating an SBP via investment casting in a domestic foundry. Nondestructive testing based on X-ray analysis was used to assess the efficacy of the proposed scheme in preventing the formation of casting defects.

MATERIALS AND METHODS

Material properties and gating systems

The SBP in this study was cast in SUS304 alloy with the following composition: C (≤ 0.08 %), Si (≤ 1.00～0.35 %), Cr (17.00～19.00 %), Mn (≤ 2.00 %), Ni (8.00-11.00 %), P (≤ 0.030 %), and S (≤ 0.030 %). Note that SUS304 alloy provides good corrosion and heat resistance as well as good mechanical strength at low temperatures. The thermo-physical properties of SUS304 alloy are as follows: density (7930 kg/m^3), specific heat (500 $J/kg \cdot K$), heat conductivity (16.3 $W/m \cdot K$), latent heat (289.9 kJ/kg), liquidus temperature (1454 ℃), and solidus temperature (1399 ℃). Figures 2 (a)-(b) respectively present 3D and cross-sectional figures of an SBP with the following dimensions: outside diameter (62.4 mm), inside diameter (50.6 mm), height (132.5 mm), thickness of shell (3.5-17 mm). The total mass of the SBP was 1998 g.

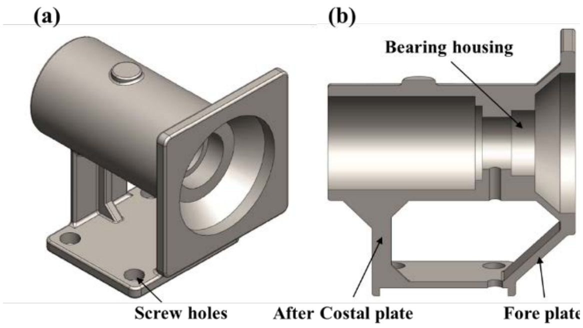

Fig. 2. Illustrations of SBP of CP: (a) 3D figure; (b) cross-sectional figure.

Figure 3 presents a schematic illustration of the preliminary gating system used to cast SBP in Case0. The dimensions of the gating system in Case0 were as follows: 80 mm (diameter of sprue cup), 300×30×25 mm (runner), 5.5×25×15 mm (Gate1), 25 (diameter)×36.5 (H) mm (Gate2), and 15×18×33.5 mm (Gate3). As shown in Fig. 4 (a)-(e), the initial analysis results obtained from Case0 were used to formulate candidate gating systems for the subsequent casting of SBPs in Case1 through Case5. In this study, we employed gravity casting with air cooling (or water cooling) using shell molds of zircon sand. As shown in Table 1, numerical simulations were conducted for each of the aforementioned casting systems under six test conditions (i.e., various ceramic shell and casting temperatures and molten metal pour rates).

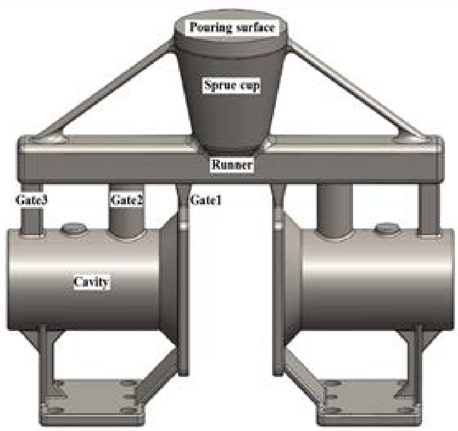

Fig. 3. Illustration of preliminary gating system (i.e., Case0).

Numerical model

Casting can be divided into two stages: filling and solidification. The underlying physical phenomena include flow, cooling, and shrinkage. The formation of shrinkage cavities and/or porosity defects during casting is generally due to non-uniformity in the cooling and solidification of the molten metal, the complex thermo-physical properties of the alloy, the geometry of the cast, and cooling conditions (Huang et al., 2020). In this study, AnyCasting software was used to conduct simulations on the investment casting of an SBP. Hexahedral elements of appropriate size were used to mesh the casting systems. Calculations pertaining to the pressure field, velocity field, and temperature field during filling and solidification were based on the continuity equation, Navier-Stokes equation, energy conservation, the volume of fluid (VOF) function, and k-ε equations (User manual of AnyCasting, 2001; Huang et al., 2019; Hirt and Nichols, 1981; Nichols and Hirt, 1975).

The following continuity equation was used to calculate the conservation of mass associated with the molten metal used to fill the cavity:

$$\frac{\partial \rho}{\partial t} + \nabla \cdot (\rho \vec{u}) = 0 \tag{1}$$

In Eq. (1), ρ and t respectively denote fluid density and time, and $\vec{u}$ indicates the velocity vector.

The Navier-stokes equation was used to calculate pressure and velocity fields of molten metal, as follows:

$$\rho \frac{\partial \vec{u}}{\partial t} + \rho \vec{u} \cdot \nabla \vec{u} = -\nabla P + \mu \nabla^2 \vec{u} + \rho \vec{g} \ . \tag{2}$$

where P and μ respectively refer to the pressure and dynamic viscosity of molten metal, and $\vec{g}$ refers to gravitational acceleration.

The energy conservation equation was used to calculate the temperature field and process of molten metal solidification, as follows:

$$\rho \frac{\partial H}{\partial t} + \rho H \nabla \cdot \vec{u} - \nabla \cdot (k \nabla T) - q = 0 \ . \tag{3}$$

where H and q respectively refer to enthalpy and volumetric heat flux.

The volume function equation was used in conjunction with the Navier-stokes equation to determine the flow patterns of molten metal in a non-fixed direction at the free boundary, as follows:

$$\frac{\partial F_v}{\partial t} + \vec{u} \cdot \nabla F_v = 0 \ . \tag{4}$$

where F_v refers to the volume-of-fluid function. In cases where a calculation cell was empty (i.e., no fluid inside), the F_v value was set at zero, and when a cell was full, the F_v value was set at 1 (Huang et al., 2020; Huang and Lin, 2015; Nichols and Hirt, 1980; Chen and Raad, 1997).

Conventional $k - \varepsilon$ equations were used to account for the evolution of turbulent flow, as follows:

$$\frac{\partial k_e}{\partial t} + u_j \frac{\partial k_e}{\partial x_j} = \frac{\partial}{\partial x_j}\left[\left(u + \frac{u_t}{\sigma_k}\right)\frac{\partial k_e}{\partial x_j}\right] + P_{ke} - \varepsilon \ , \tag{5}$$

$$\frac{\partial \varepsilon}{\partial t} + u_j \frac{\partial \varepsilon}{\partial x_j} = \frac{\partial}{\partial x_j}\left[\left(u + \frac{u_t}{\sigma_\varepsilon}\right)\frac{\partial \varepsilon}{\partial x_j}\right] + c_{\varepsilon 1} P_k \frac{\varepsilon}{k_e} - c_{\varepsilon 2}\frac{\varepsilon^2}{k_e} \tag{6}$$

where u_j, ε, and k_e respectively refer to velocity components in the corresponding direction, the dissipation rate of turbulence kinetic energy, and

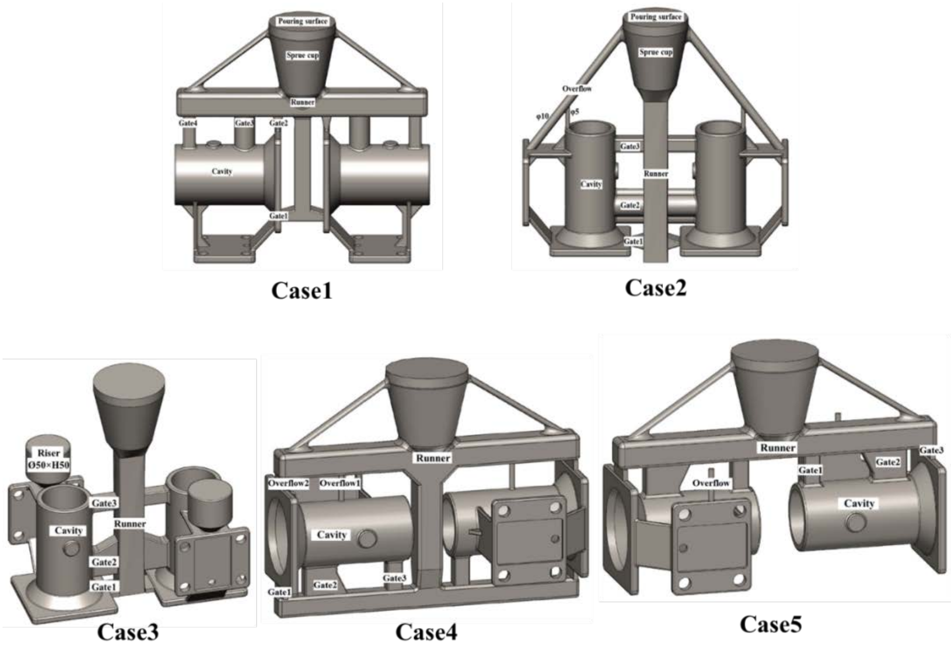

Fig. 4. Illustrations of gating systems in Case1 to Case5.

turbulence kinetic energy. Symbols σ_k and σ_ε respectively indicate the Prandtl numbers corresponding to turbulence kinetic energy (k_e) and the rate of dissipation (ε). Symbol u_t indicates turbulence eddy viscosity, which is derived as follows:

$$u_t = \frac{\rho C_\mu k_e^2}{\varepsilon} \quad (7)$$

where the values of the constants used in the turbulence model were as follows: C_μ = 0.09, σ_k = 1.00, σ_ε = 1.30, $C_{\varepsilon 1}$ = 1.44, and $C_{\varepsilon 2}$ = 1.92 (Huang et al., 2020).

For each casting system, a statistical RMM model was used to evaluate the probability of cavity shrinkage formation, as follows (Huang et al., 2020; User manual of AnyCasting, 2001):

$$M_R = V_R \;/\; S_R \quad (8)$$

where V_R and S_R respectively refer to the volume and surface area of an isolated melt at the time that each mesh reached the critical solid fraction. Note that a smaller RMM value corresponds to a higher likelihood of defect formation (Huang et al., 2020; User manual of AnyCasting, 2001).

The dynamic solidification behavior of the molten metal in the cavity was determined using Eqs. (1)-(8). AnyCasting was used to solve differential equations and analyze flow through the mold based on the finite difference method. This approach is superior to other numerical methods in terms of convergence speed and iterative computation. Convergence tests were used to determine the optimal number of grids in the casting system (approximately 2,955,186 elements).

Table 1 Experiment and simulation conditions for each of the casting schemes

	Exp1	Exp2	Exp3	Exp4	Exp5	Exp6
Casting material			SUS304			
Shell mold material			Zircon Sand			
$T_{ceramic}$ (°C)	1050	1100	1150	1050	1100	1150
$T_{casting}$ (°C)	1600	1600	1600	1650	1650	1650
t_{pouring} (s)	6	6	6	9	9	9
δ (mm)			6			

Note: $T_{ceramic}$, $T_{casting}$, t_{pouring}, and δ represent temperature of ceramic shell, temperature of casting, period of pouring molten metal, and shell thickness, respectively.

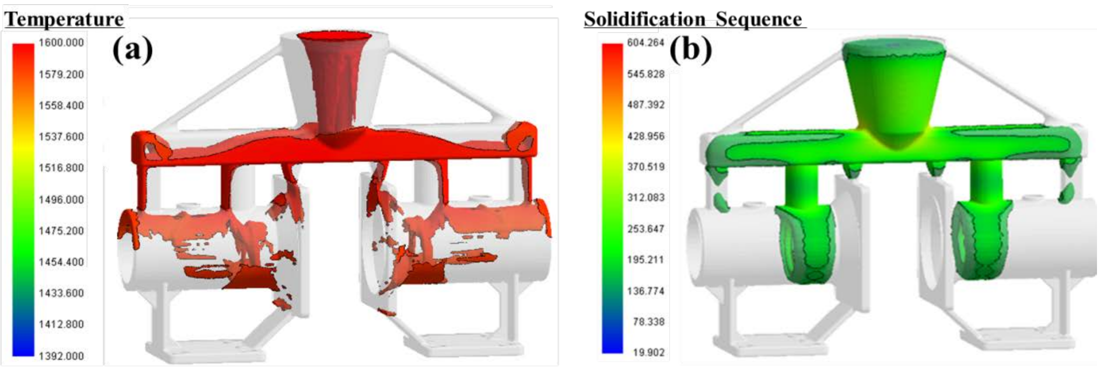

Figure 5 Numerical simulations of gating system under Case0-Exp2: (a) at t=1.2 s from the beginning of filling, (b) at t = 196.82 s from the beginning of solidification.

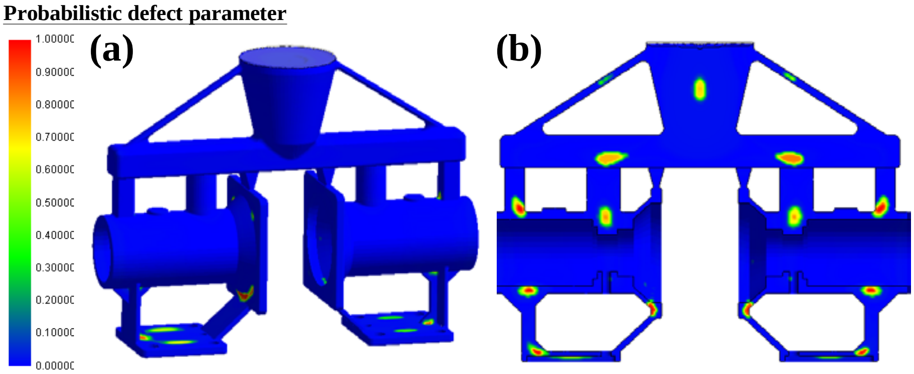

Figure 6 Prediction of shrinkage cavity based on RMM for the gating system under Case0-Exp2: (a) isometric view; (b) front cross-sectional view.

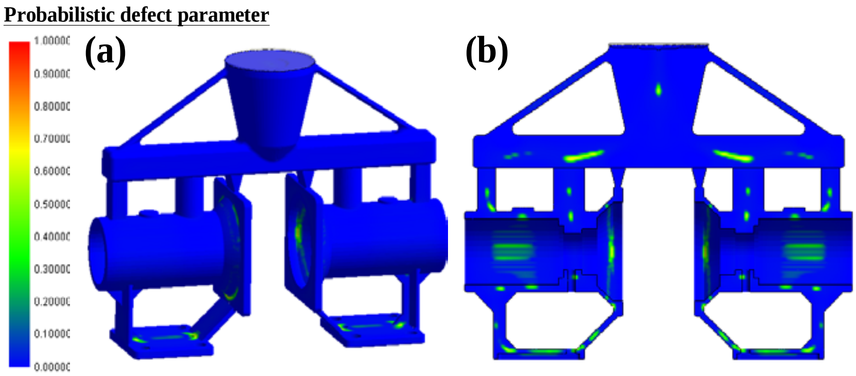

Figure 7 Prediction of porosity defect formation based on Niyama criterion for the gating system under Case0-Exp2: (a) isometric view; (b) front cross-sectional view.

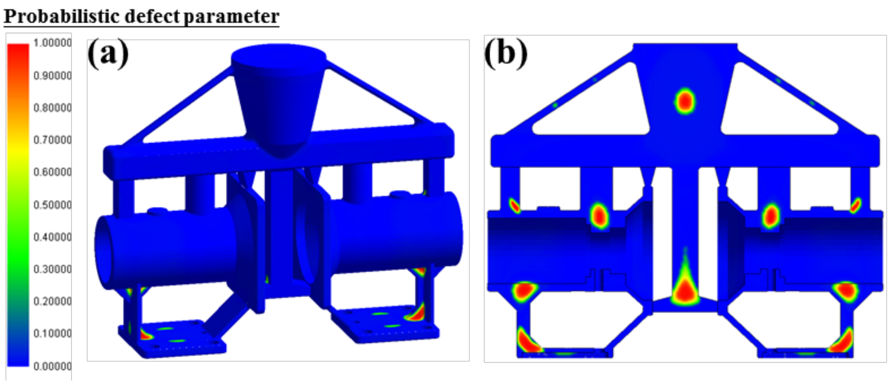

Figure 8 Prediction of shrinkage cavity based on RMM for the gating system under Case1-Exp6: (a) isometric view; (b) front cross-sectional view.

RESULTS AND DISCUSSION

Preliminary casting scheme (Case0-Exp2)

The following numerical simulations were based on the test conditions outlined in Exp2, which are commonly used in the manufacturing of SBP in industrial foundries. Figures 5(a)-(b) present numerical simulations of the gating system under Case0-Exp2 at two points in time: (a) at t=1.2 s from the beginning of filling, and (b) at t = 196.82 s from the beginning of solidification. Note that in this case, the filling and solidification processes were respectively completed in 6 s and 545 s. Fig. 5(b) reveal the formation of isolated molten metal in Gate3 at t = 196.82 s (due to an insufficient pour), which greatly increases the likelihood of cavity shrinkage. Note that the objective underlying the design of Case0 (used in many domestic foundries) is to ensure the filling of the mold with molten metal and to facilitate the handling of the finished cast product. In other words, this design protocol does not account for the flow of molten metal through the cavity or the direction of solidification.

This study used the probabilistic defect parameter (PDP), based on RMM (or the Niyama criterion), which is dimensionless with a value ranging from 1.0 (highest likelihood) to 0.0 (lowest likelihood). Figures 6(a)-(b) illustrate predictions of the shrinkage cavity based on RMM using the gating system under Case0-Exp2: (a) isometric view and (b) front cross-sectional view. These figures reveal the casting defects with the highest likelihood of occurring (shown in red) at the runner, at the junction between the Gate3 and the stuffing box, and at the junction between the stuffing box and pedestal. Figures 7(a)-(b) illustrate the prediction of porosity defect based on the Niyama criterion for the gating system under Case0-Exp2: (a) isometric view and (b) front cross-sectional view. Note that in these images the areas with a low likelihood of porosity defect are indicated in green. Note that in these images the areas with a low likelihood of porosity defect are indicated in green. The consistency between the numerical simulations in Fig. 6 and the experiment results in Fig. 1 demonstrates the accuracy of the proposed numerical model.

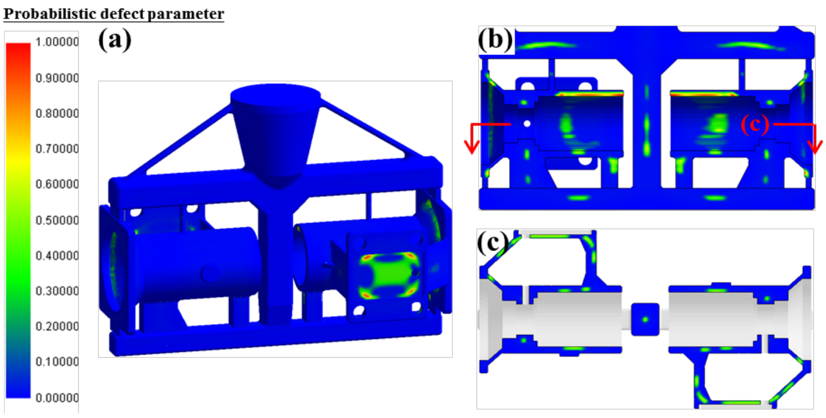

Figure 9 Prediction of porosity defect formation based on Niyama criterion for the gating system under Case4-Exp5: (a) isometric view; (b) front cross-sectional view; (c) top cross-sectional view (section “c-c”).

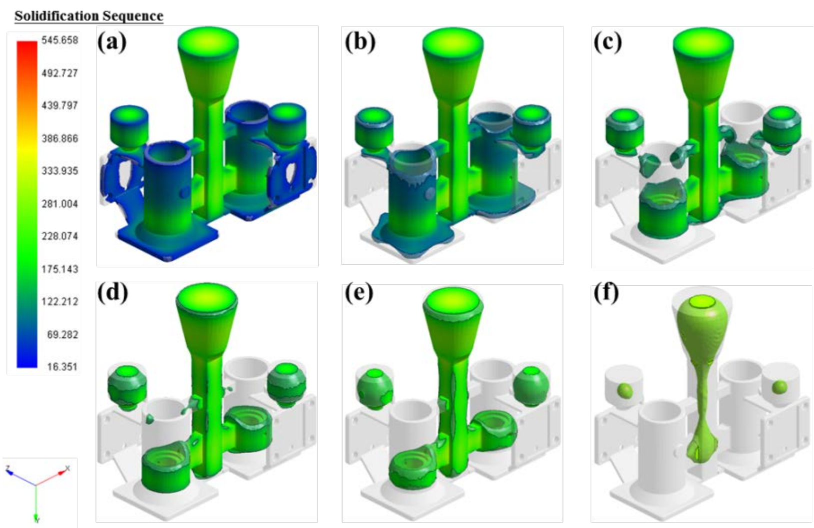

Figure 10 Numerical simulations of solidification process of gating system under Case3-Exp1: (a) at 42.81 s, (b) at 85.16 s, (c) at 116.91 s, (d) at 143.38 s, (e) at 169.84 s, (f) at 286.29 s.

Numerical simulations of Case1 to Case5

As shown in Fig. 4, we formulated five new schemes for the casting of SBPs based on the results obtained from Case0-Exp2. A number of design concepts were incorporated within the candidate casting schemes: addition of vertical runner and side-gate (Case1), rearrangement of casting tree for side-gating (Case2), addition of riser (Ø50×H50 mm) to Case2 (Case3), adoption of bottom-gating scheme (Case4), and bottom-gating scheme in Case4 inverted to operate as top-gating scheme (Case5). Note that the objective behind the addition of a riser was to vent exhaust gas and slag, while minimizing the shrinkage of molten metal in the mold during solidification.

Numerical simulations in Case1, Case2, and Case4

Figures 8(a)-(b) illustrate the predictions pertaining to the shrinkage cavity, based on RMM for the gating system in Case1-Exp6: (a) isometric view and (b) front cross-sectional view. Comparing the results in Case1-Exp6 (Fig. 8) with those in Case0-Exp2 (Fig. 6) revealed the following insights. (1) The adoption of a vertical runner in Case1 decreased the PDP value at the joint between the stuffing box and fore-pedestal from 1.0 (in Case0-Exp2) to 0.0 (in Case1-Exp6), indicating that the likelihood of shrinkage cavity formation in that area was essentially nil. (2) Note however that this casting configuration increased the PDP value in the bearing housing to 1.0, indicating a very high likelihood of shrinkage cavity formation in that area. (3) As for the likelihood of shrinkage cavity formation in other locations, Case1-Exp6 and Case0-Exp2 were essentially the same. Note that in the case with a vertical runner and side-gating scheme (Case2-Exp6), the PDP distribution of shrinkage cavity formation (based on RMM) was very similar to that in Case1-Exp6.

Figures 9(a)-(c) present predictions pertaining to the formation of porosity defects based on the Niyama criterion for the gating system under Case4-Exp5: (a) isometric view, (b) front cross-sectional view, and (c) top cross-sectional view (section “c-c”). The regions most likely to be affected by porosity defects were at the baseplate of the SBP and the cylindrical shell of stuffing box, as indicated in red in the figures. These porosity defects result from poor exhaust from the baseplate and the cylindrical shell of SBP. Overall, the results obtained from Case1, Case2, and Case4 indicate that the likelihood of shrinkage cavities and porosity defects could both be reduced by making adjustments to the gating system.

Numerical simulations in Case3 and Case5

We sought to improve on the gating system in Case2 by adding a riser (Ø50×H50 mm) (i.e., Case3). Figures 10(a)-(f) present numerical simulations of the solidification process using the gating system designed for Case3-Exp1: (a) at 42.81 s, (b) at 85.16 s, (c) at 116.91 s, (d) at 143.38 s, (e) at 169.84 s, and (f) at 286.29 s. In Case3-Exp1, the process of solidification required 545 s. The riser in Case3 provided a source of additional molten metal to prevent the isolation of molten metal in the back-pedestal at 169.84 s (Fig. 8(e)), thereby minimizing the likelihood of a shrinkage cavity forming at the joint between the back-pedestal and SBP cylinder. Figures 11(a)-(c) present predictions pertaining to the formation of porosity defects based on the Niyama criterion for the gating system under Case3-Exp1: (a) isometric view, (b) front cross-sectional view, and (c) side cross-sectional view (section “c-c”). The regions most likely to be affected by porosity defects were at the baseplate of the SBP due to poor venting, as indicated in red in the above figures.

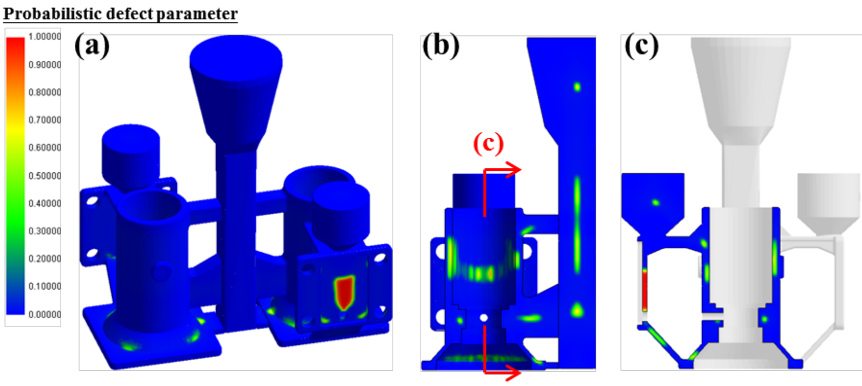

Figure 11 Prediction of porosity defect formation based on Niyama criterion for the gating system under Case3-Exp1: (a) isometric view; (b) front cross-sectional view; (c) side cross-sectional view (section “c-c”).

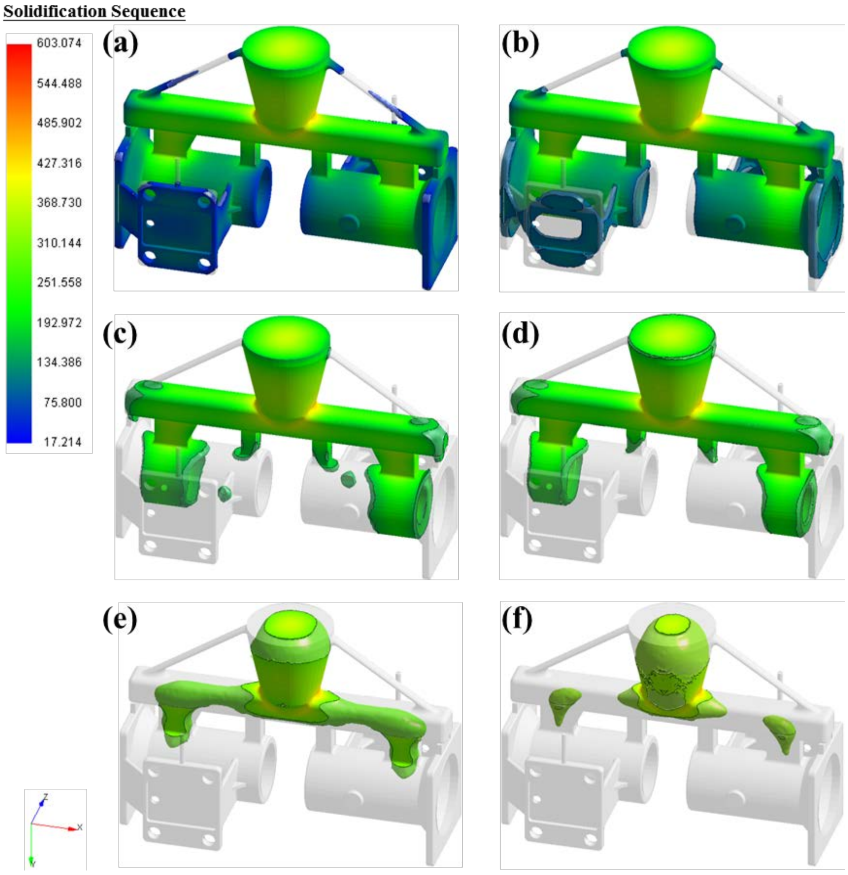

Figure 12 Numerical simulations of solidification process of gating system under Case5-Exp5: (a) 46.5 s, (b) 93.37 s, (c) 163.67 s, (d) 181.25 s, (e) 286.7 s, (f) 327.71 s.

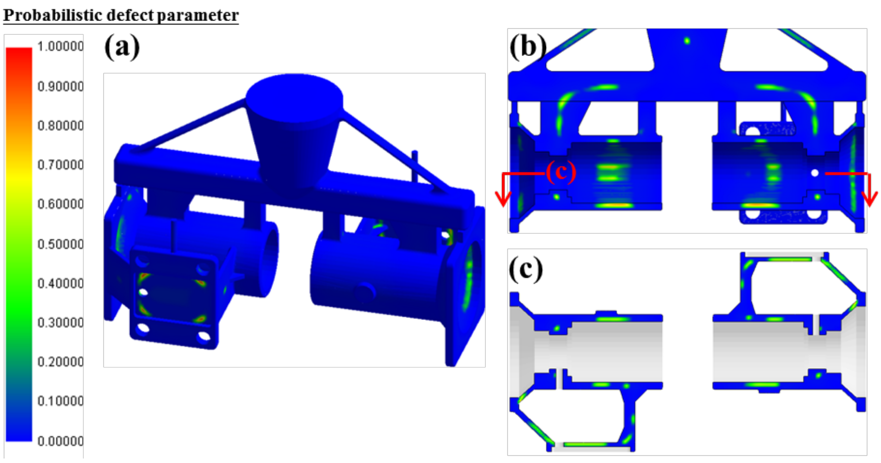

Figure 13 Prediction of porosity defect formation based on Niyama criterion for the gating system under Case5-Exp5: (a) isometric view; (b) front cross-sectional view; (c) top cross-sectional view (section "c-c").

We sought to improve the gating system in Case4 by switching from a bottom-gating scheme to top-gating scheme (i.e., Case5). Figures 12 (a)-(f) present numerical simulations of the solidification process using the gating system under Case5-Exp5: (a) 46.5 s, (b) 93.37 s, (c) 163.67 s, (d) 181.25 s, (e) 286.7 s, and (f) 327.71 s. In Case5-Exp5, the process of solidification required 603 s. Figure 12 (c) shows the isolation of molten metal in the back-pedestal at 163.67 s; however, replenishment from Gate1 had eliminated the isolation of molten metal at 181.25 s (Fig. 12(d)), which greatly reduced the likelihood of shrinkage cavity formation in that area. Figure 13(a)-(c) present predictions pertaining to the formation of porosity defects based on the Niyama criterion for the gating system under Case5-Exp5: (a) isometric view, (b) front cross-sectional view, and (c) top cross-sectional view (section "c-c"). In the figures, the regions most likely to be affected by porosity defects formation are indicated in green.

Virtual thermo-dynamic sensors

Figures 14(a)-(c) present schematic illustrations showing the positions of the virtual thermo-dynamic sensor (VTDS): (a) Case0, (b) Case3, and (c) Case5. Figure 14(d) presents the temperature variations in the molten metal at the VTDS as a function of time under Case0 (red curve), Case3 (green curve), and Case5 (black curve). Fig. 14(e) presents temperature variations in the molten metal at the VTDS with the solidification fraction (S_r) under Case0, Case3, and Case5. In Fig. 14(d)-(e), solid and dashed curves represent VTDS-A (in the bearing housing) and VTDS-B (in the back-pedestal), respectively. The gating temperatures used in the numerical simulations were as follows: 1600 °C (Case0-Exp2 & Case3-Exp1) and 1650 °C (Case5-Exp5).

The results in Fig. 14(d) reveal the following important findings: (1) At VTDS-A, the time required for molten metal to reach the solidus temperature of the alloy (1399 °C) from the liquidus temperature (1454 °C) was as follows: 323.8 s (Case0-Exp2)、335.7 s (Case3-Exp1), and 360.3 s (Case5-Exp5). The time difference indicates that the higher gating temperature delayed solidification by 36.5 s (comparing with Case0-Exp2) and 24.6 s (Case3-Exp1), thereby allowing a sufficient flow of molten metal into the mold cavity, which greatly decreased the likelihood of shrinkage cavity and/or porosity defect formation. (2) At VTDS-B, the time required for the molten metal to reach the solidus temperature from the liquidus temperature was as follows: 152 s (Case0-Exp2) and 200 s (Case3-Exp1 & Case5-Exp5). The results in Fig. 14(e) reveal that at VTDS-A, the value of S_r reached to 80% under Case0-Exp2, Case3-Exp1, and Case5-Exp5, when the temperature of molten metal lowered the solidus temperature of the alloy (1399 °C).

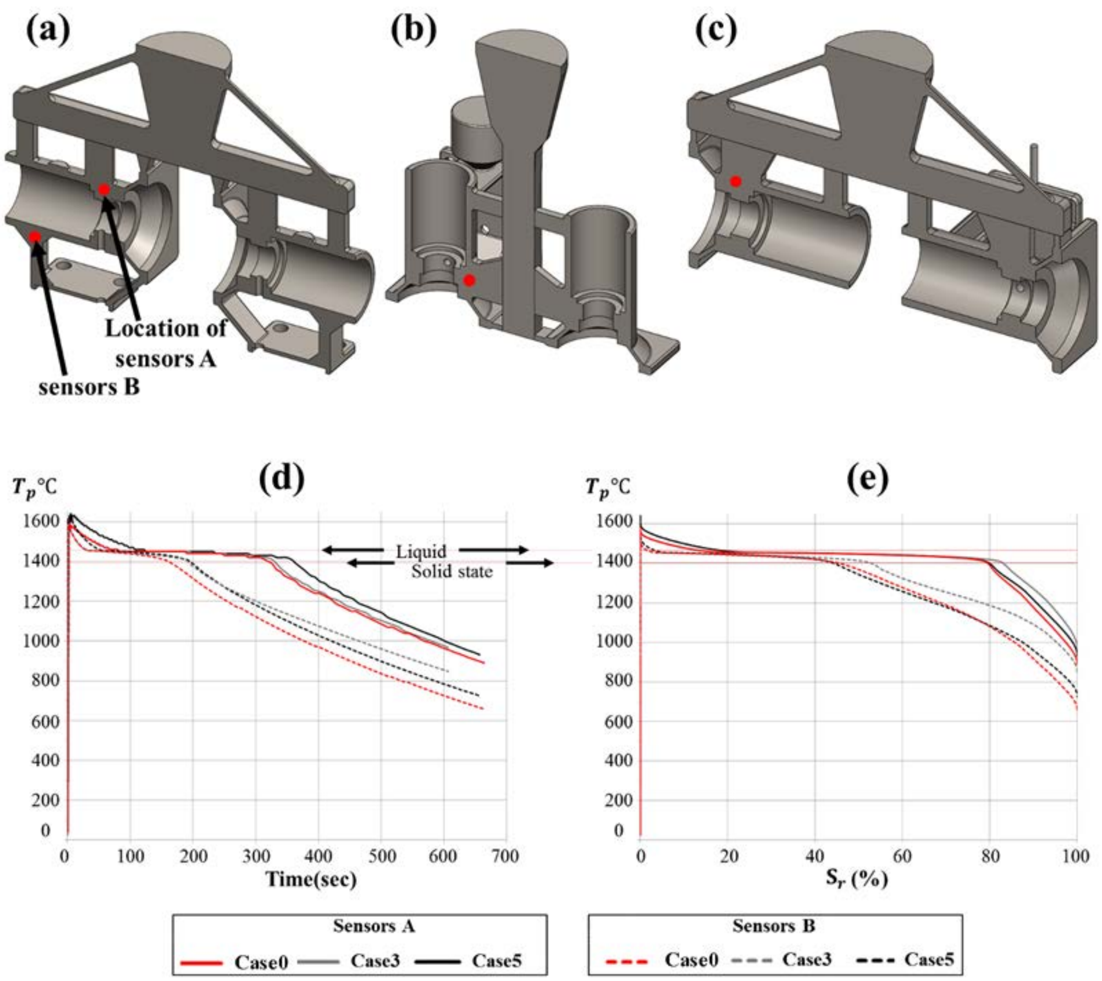

Figures 14(a)-(c) Schematic illustrations showing the positions of the virtual thermo-dynamic sensor (VTDS) for Case0, Case3, and Case5, respectively; (d) temperature variations in the molten metal at VTDS as a function of time under Case0, Case3, and Case5; (e) temperature variations in the molten metal at the VTDS with the solidification fraction (S_r) under Case0, Case3, and Case5.

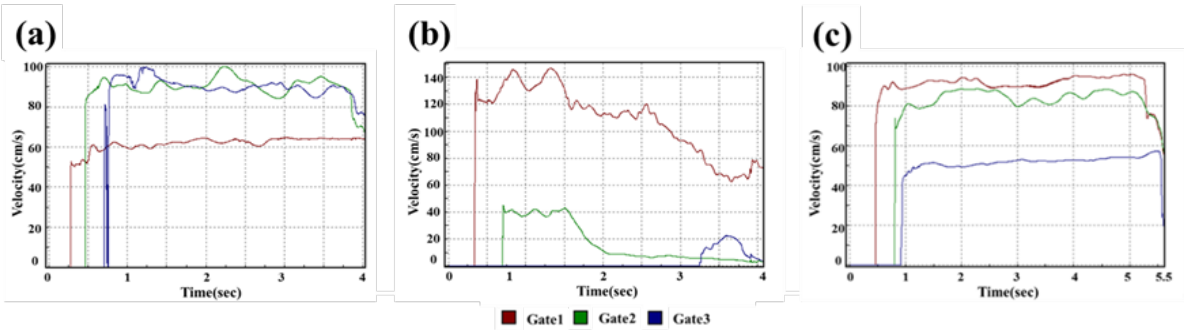

Figure 15(a)-(c) Variations in the velocity of the molten metal at the inlet of gating systems as a function of time: (a) Case0-Exp2; (b) Case3-Exp1; (c) Case5-Exp5.

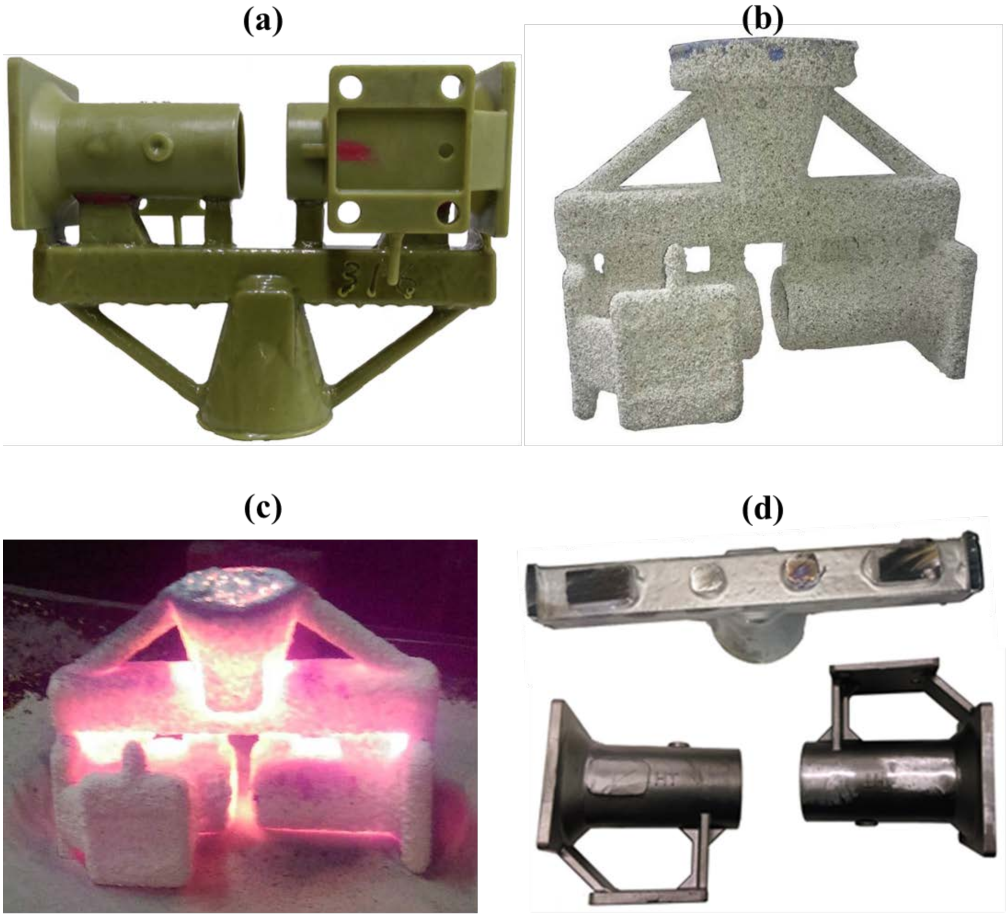

Figure 16(a)-(d) Photographs of casting in Case5-Exp5: (a) wax tree; (b) ceramic shell mold; (c) ceramic shell mold after filling molten metal (under air cooling); (d) finished product of SBP and runner.

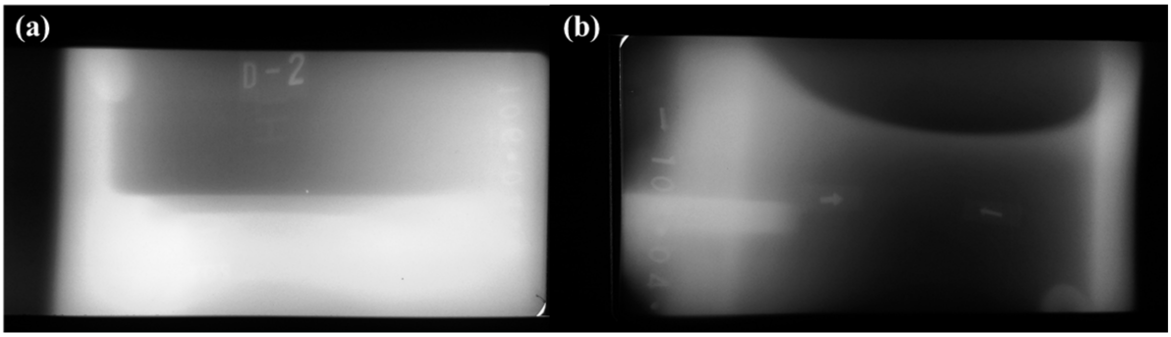

Figure 17(a)-(b) X-ray images of casting in Case5-Exp5: (a) bearing housing; (b) SBP cylinder.

Velocity of molten metal at inlets of the gating system

Figures 15(a)-(c) present variations in the velocity of the molten metal at the inlet of the gating system as a function of time: (a) Case0-Exp2, (b) Case3-Exp1, and (c) Case5-Exp5. The three curves in Fig. 15 respectively indicate the velocities at various inlets of the gating system: brown curve (Gate1), green curve (Gate2), and blue curve (Gate3). During the filling process, there were more changes in the velocity values at Gate1, Gate2, and Gate3 under Case0-Exp2 than under Case5-Exp5. The average velocity values at the inlets under Case5-Exp5 were as follows: 90 cm/s (Gate1), 85 cm/s (Gate2), and 53 cm/s (Gate3), as shown in Fig. 15(c). This is an indication that the steady flow of molten metal can supress the occurrence of turbulence as well as the formation of pores and slag in the mold cavity.

Based on the overall results, we determined that the optimal casting conditions for the fabrication of SBP were those used in Case5-Exp5: Case5 gating system, casting temperature = 1650 °C, ceramic shell temperature = 1100 °C, filling period = 9 s, and ceramic shell thickness = 6.0 mm.

Experiment verification

To verify the accuracy of the simulations, an SBP was fabricated via investment casting in an industrial foundry using the optimal parameter set. Nondestructive radiographic testing (RT) was used to assess the efficacy of the optimized casting conditions in preventing casting defects. Figures 16(a)-(d) present photographs of the casting obtained using the parameters in Case5-Exp5: (a) wax tree, (b) ceramic shell mold, (c) ceramic shell mold after filling molten metal (under air cooling), and (d) finished product of SBP and runner.

Figures 17(a)-(b) present X-ray images of casting obtained using the parameters in Case5-Exp5: (a) bearing housing and (b) cylinder of SBP. No obvious cavity shrinkage was observed at the surface of the finished product. Nondestructive RT analysis revealed no black spots inside the SBP. The quality of the finished product provides evidence that supports the efficacy of the proposed strategy for the casting of SBP.

CONCLUSIONS

This study reports on the use of the AnyCasting software package in conjunction with RMM to predict the occurrence of shrinkage cavities, as well as Niyama criterion to predict the occurrence of porosity defects in the casting of an SBP. Results obtained from preliminary simulations and experiments were used to formulate five casting schemes. VTDSs were used to simulate the casting systems with a particular focus on the rate and direction of solidification in various regions of the cast. We also investigated variations in the velocity of the molten metal at the inlets of the gating system over time. The optimal casting parameters were then used in the fabrication of an SBP in an industrial foundry: Case5 gating system, casting temperature = 1650 °C, ceramic shell temperature = 1100 °C, filling period = 9 s, and ceramic shell thickness = 6.0 mm. Nondestructive RT analysis revealed that the proposed casting scheme and casting parameters eliminated most of the detrimental casting defects commonly associated with this type of casting. The strategy presented in this paper provides a valuable reference for the investment casting of SBP from the perspective of quality as well as cost efficiency. Importantly, the optimal casting conditions derived in this study improved the manufacturing process in terms of product quality, time-consumption, and cost.

ACKNOWLEDGMENT

The authors gratefully acknowledge the support provided for this research by the Ministry of Science and Technology, R.O.C. under grants MOST 108-2221-E-224-034 and MOST 108-2622-E-224-016-CC3.

REFERENCES

Beckermann, C. and Carlson, K., “Use of the Niyama criterion to predict shrinkage-related leaks in high-nickel steel and nickel-based alloy castings,” Department of Mechanical and Industrial Engineering, The University of Iowa (2008).

Birajdar, R., Patil, R. and Khanzode, K., “Vibration and noise in centrifugal pumps-source and diagnosis methods,” Proc of 3rd Int Conf on Integrity, Reliability and Failure, Porto/Portugal, July 20-24 (Paper Ref: S1163_P0437) (2009).

Budavari, I. and Molnar, D., “Control volume simulation of casting directional solidification,” Mater. Sci. Forum, Vol.790–791, pp.146–151 (2014).

Chen, S. and Raad, D.B., “The surface marker and micro-cell method,” Int. J. Numer. Methods Fluids, Vol.25, pp.749–778 (1997).

Forsthoffer, W.E., “Pump best practices,” Forsthoffer's Best Practice Handbook for Rotating Machinery, PP.25–91 (2011).

Groover, M.P., *Fundamentals of Modern Manufacturing 3/e Materials, Processes, and Systems,* John Wiley & Sons Inc. pp.39–57 (2007).

Guo, J., Beckermann, C., Carlson, K., Hirvo, D., Bell, K., Moreland, T., Gu, J., Clews, J., Scott, S., Couturier, G. and Backman, D., “Microporosity prediction and validation for

Ni-based superalloy castings," Mater. Sci. Eng., Vol.84, pp.1–5 (2015).
Hirt, C.W. and Nichols, B.D., "Volume of fluid (VOF) method for the dynamics of free boundaries," J. Comp. Phys., Vol.39, pp.201–225 (1981).
Huang, P.H., Luo, J.Y., Hung, S.C., Lin, C.J. and Cheng, H.H., "Optimal pouring system design for investment casting of cladding thin-plate heater using metallic mold flow analyses," Appl. Mech. Mater., Vol.627, pp. 46–49 (2014).
Huang, P.H. and Guo, M.J., "A study on the investment casting of 17-4PH stainless steel helical impeller of centrifugal pump," Mater. Res. Innov., Vol.19, No.S9, PP.77–81 (2015).
Huang, P.H. and Lin, C.J., "Computer-aided modeling and experimental verification of optimal gating system design for investment casting of precision rotor," Int. J. Adv. Manuf. Technol., Vol.79, pp.997–1006 (2015).
Huang, P.H., Shih, L. K.L., Lin, H.M., Chu, C.I. and Chou, C.S., "Novel approach to investment casting of heat-resistant steel turbine blades for aircraft engines," Int. J. Adv. Manuf. Technol., Vol.104, pp.2911–2923 (2019).
Huang, P.H., Cheng, C.Y., Huang, W.J. and Chou, C.S., "Optimal design of investment casting system for toothed chain joint: Computer simulations and experimental verification," Int. J. Adv. Manuf. Technol., Vol.106, pp.1931–1943 (2020).
Kalpakjian, S. and Schmid, S., *Manufacturing Engineering & Technology* (5th Edition), Pearson Education, NJ, pp.292–317 (2003).
Kim, K.H., Hwang, J.H., Oh, J.S., Lee, D.H., Kim, I.H. and Yoon, Y.C., "Prediction of shrinkage defect in steel casting for marine engine cylinder cover by numerical analysis," World Foundry Congress (WFC06), Vol.209, PP.1–9 (2005).
Kuo, J.K., Huang, P.H., Lai, H.Y. and Chen, J.R., "Optimal gating system design for investment casting of 17-4PH stainless steel enclosed impeller by numerical simulation and experimental verification," Int. J. Adv. Manuf. Technol., Vol.92, pp.1093–1103 (2017).
Kuo, J.K., Huang, P.H., Lai, H.Y. and Wu, W.J., "Design of casting systems for stainless steel exhaust manifold based on defective prediction model and experimental verification," Int. J. Adv. Manuf. Technol., Vol.100, pp.529–540 (2019).
Liao, D.M., Chen, L.L., Zhou, J.X. and Liu, R.X., "Numerical simulation of thermal stress fields of steel casting," Adv. Mat. Res., Vol.179–180, PP.1118–1123 (2011).
Matlakala, M.E., Kallon, D.V.V., Simelane, S.P. and Mashinini, P.M., "Impact of design parameters on the performance of centrifugal pumps," Procedia Manuf., Vol.35, pp. 197–206 (2019).
Moroe, T.R. and Palmer, K., "Prefilled equipment baseplate – How to get a superior equipment installation for less money," Proc. of 19th Int. pump users symposium (2002).
Nichols, B.D. and Hirt, C.W., "Methods for calculating multidimensional, transient free surface flows past bodies," Proc. of 1st Int. Conf. on Num. Ship Hydrodynamics, Gaithersburg, ML, Oct 20–23 (1975).
Nichols, B.D. and Hirt, C.W., "Numerical simulation of BWR ventclearing hydrodynamics," Nucl. Sci. Eng., Vol.73, No.2, pp.196–209 (1980).
Niyama, E., Uchida, T., Morikaya, M. and Siato, S., "A method of shrinkage prediction and its application to steel casting practice," Am Foundrymen's Soc. Int. Cast. Met. J., Vol.7, No.3, pp.52–63 (1982).
Rushabh, S., Akash, S. and Tejas, "Design and analysis of baseplate of centrifugal pump," Int. J. Adv. Res. Ideas Innovat. Technol., Vol.3, No.2, pp.837–838 (2017).
Sanders, R.E., "Accidents involving compressors, hoses, and pumps," Chemical Process Safety (4th Edition), pp.235–267 (2015).
User manual of AnyCasting, version 6.0, AnyCasting, Co., Ltd. Gangseo-gu, Seoul City (2001).
Zhang, X.P. and Chen, G., "Computer simulation of the solidification of cast titanium dental prostheses," J. Mater. Sci., Vol.40, pp.4911–4916 (2005).
Zhou, J.X., Liu, R.X., Chen, L.L. and Liao, D.M., "Applications of foundry CAE in steel casting," Hot Work Technol., Vol.42, No.15, pp.80–85 (2004)

基於數值模擬與實驗研究之泵浦底座澆鑄系統設計

郭振坤
國立台南大學綠色能源科技學系

黃培興
國立雲林科技大學機械工程系

蔡鈺鼎
逢甲大學精密系統設計學士學位學程

鍾齊　周春禧
國立屏東科技大學機械工程系

摘 要

帶填料函的基座是離心泵的主要組成部件。它負責將離心泵產生的負載移轉到泵的底板及地基上，通常採用熔模鑄造製造。但是此工藝容易產生殘餘鑄造缺陷，因而降低機械強度並增加長期使用後形成裂紋的可能性。本研究基於有限差分法之電腦輔助金屬模流分析技術，針對改善精密鑄造中常見之巨觀縮孔、微觀縮鬆與氣孔缺陷，於 SUS304 不銹鋼泵浦底座產品之澆鑄系統優化設計。初步模擬和實驗的結果為隨後的模擬提供了五個鑄造方案的建立。我們使用虛擬的熱力學傳感器來確定型腔中鐵水的凝固速率和方向，並且還研究了澆口系統入口處的熔融金屬速度隨時間的變化，通過在國內鑄造廠之驗證獲得熔模鑄造 SBP 製程之最佳鑄造參數。